Available online at www.sciencedirect.com
ScienceDirect
Trans. Nonferrous Met. Soc. China 32(2022) 4014−4029
Transactions of Nonferrous Metals Society of China
www.tnmsc.cn

CMAS corrosion resistance characteristics of $RE_{50}Ta_xZr_{50-x}O_{175+0.5x}$ thermal barrier oxides in $RE_2Zr_2O_7$−$RETaO_4$ systems

Shan-shan GONG, Ming CHEN, Xun-peng HUANG, Fan ZHANG

School of Materials Science and Engineering, Xiangtan University, Xiangtan 411105, China

Received 18 September 2021; accepted 22 December 2021

Abstract: The corrosion resistance characteristics of RE-rich $RE_{50}Ta_xZr_{50-x}O_{175+0.5x}$ oxides in $RE_2Zr_2O_7$−$RETaO_4$ systems to calcium−magnesium−alumino−silicate (CMAS) at 1300 °C, and the influence of RE^{3+} and Ta^{5+} on chemical reactions and reactive crystallization of CMAS melts were investigated. The results show that following the thermochemical reactions, apatite, pyrochlore, reprecipitated fluorite and residual $Yb(Y)TaO_4$ phases were the predominant reaction products. Formation abilities of apatite and pyrochlore were found to be proportional to the ionic radius of RE^{3+}. The increase of Ta^{5+} amount can decrease the number of available RE^{3+} to form apatite. Moreover, the resistance characteristic to CMAS corrosion in $RE_{50}Ta_xZr_{50-x}O_{175+0.5x}$ systems was decided by the combined action of apatite and pyrochlore phases. The cohesive mixture of apatite and pyrochlore phases can generate a dense layer near the reaction front, which had a positive effect on suppressing CMAS infiltration. The ability of the fluorite + $RETaO_4$ two-phase field was determined to be sufficient to mitigate CMAS corrosion.

Key words: thermal barrier coatings; CMAS corrosion; thermochemical reaction; apatite; pyrochlore; penetration experiment

---

1 Introduction

Thermal barrier coatings (TBCs) are widely applied to modern turbine engines to protect hot-section metallic structures [1−3]. The 7−8 wt.% Y_2O_3 (7.6−8.7 mol.% $YO_{1.5}$) stabilized zirconia (7−8 YSZ) [4−6] is widely used as the ceramic top coating of TBCs in advanced gas turbine engines due to its superior durability in thermal cycling [7]. However, the application of traditional YSZ is limited at higher operating temperatures (>1200 °C) expected in future engines. One of the main issues is that the YSZ coatings have become increasingly susceptible to environmental degradation [8−10] by calcium−magnesium−alumino−silicate (CMAS) at high temperatures. Depending on the specific service environment, the molten deposits contain CaO, MgO, $AlO_{1.5}$, SiO_2, FeO_x and other minor components with a range of composition variations [11]. The molten glass can penetrate into YSZ TBCs and result in the loss of strain tolerance and spallation [12−14].

In order to obtain an effective CMAS mitigation strategy, a series of investigations about the possible chemical reactions between candidate thermal barrier oxides (TBO) and CMAS melt have been reported [15−17]. In the absence of any chemical interactions, it is conceivable that the CMAS melt flow might be arrested when its viscosity increases [18] or its temperature decreases to the onset of rapid intrinsic crystallization [10,19]. In the case of the occurrence of chemical reactions, the crystallization of one or more products can be induced. These contain reprecipitation of the TBO with a modified composition and/or structure [20], crystallization of a reaction product [21,22] and intrinsic crystallization of the residual melt [20,21].

Corresponding author: Fan ZHANG, Tel: +86-731-58292064, E-mail: zhangfan15@xtu.edu.cn
DOI: 10.1016/S1003-6326(22)66074-6

The reactive crystallization scenario is considered to be the most effective approach to prevent the CMAS penetration. Prior experiments on TBO−CMAS interactions [21,23] have shown that apatite phase is an effective crystallization for CMAS mitigation. The apatite structure, nominally $(RE,Ca,Zr)_{10}(SiO_4)_6O_2$, originates from the reactions between $REO_{1.5}$ from TBO (e.g. $Gd_2Zr_2O_7$ [21]) and SiO_2 and CaO from CMAS melt. Work on RE zirconates exhibits that the stability of the apatite phase decreases with the ionic size of the RE cation from La^{3+} to Yb^{3+} [23,24].

ZrO_2−$YO_{1.5}$−$TaO_{2.5}$ system is attractive as promising candidates for TBC applications [25−30]. MACAULEY et al [26] proposed that the two-phase field between fluorite and $YTaO_4$ in $Y_2Zr_2O_7$−$YTaO_4$ systems offered a possible pathway for enhancing toughness by the addition of a second phase and improving the ability of CMAS mitigation. However, CMAS resistance characteristics of the two-phase field in $Y_2Zr_2O_7$−$YTaO_4$ systems and the influences of the choice of various RE cations on the mechanism of CMAS mitigation are not clear. A more complete view is needed to understand the relevant effects of various RE cations and $TaO_{2.5}$ content. This study systematically investigates the reactive crystallization phases and the resistance characteristics to CMAS corrosion at 1300 °C while changing RE cations and $TaO_{2.5}$ content in $RE_{50}Ta_xZr_{50-x}O_{175+0.5x}$ (RE=Yb, Y, Dy, Gd; x=10, 20, 30, 40) systems. Hence, the aim of this article is to understand the effect of various RE cations on chemical interactions and reactive crystallization with model CMAS melts and examine the CMAS mitigating ability of the two-phase field of fluorite + $RETaO_4$.

2 Experimental

2.1 Synthesis of CMAS

CMAS powders with a composition of 33CaO−9MgO−$13AlO_{1.5}$−$45SiO_2$ in mole fraction (%) were selected in this study. The raw materials were weighed according to the appropriate molar ratio and mixed with ethanol. The mixtures were milled through the ball-milling process at a speed of 400 r/min for 8 h. The suspension was dried at 100 °C for 24 h. The mixed powder was then heated in a muffle furnace at 1300 °C for 4 h. After cooling to 25 °C, the glassy mixture was manually ground into a fine powder using a mortar and pestle. Finally, fine CMAS powder was obtained through a Fi500 mesh sieve filter.

2.2 Preparation of thermal barrier oxides

The $RE_{50}Ta_xZr_{50-x}O_{175+0.5x}$(RE=Yb, Y, Dy, Gd; x=10, 20, 30, 40) powders were synthesized by reverse co-precipitation [31] from precursor solutions of $ZrO(NO_3)_2$ (99.5%), $RECl_3\cdot 6H_2O$ (99.9%) and $TaCl_5$(99.9%). The accurately weighed $ZrO(NO_3)_2$, $RECl_3\cdot 6H_2O$ and $TaCl_5$ were separately dissolved in deionized (DI) water and ethanol, and then mixed to prevent hydrolysis of the $TaCl_5$. The mixed solutions were added drop-wise into ammonium hydroxide (NH_4OH) while the pH was maintained above 10 to ensure the precipitation of all the cations mixed at a molecular level. The hydroxide precipitates were separated, washed with ethanol and dried at 90 °C. Afterwards, the sample was pyrolyzed at 1200 °C to ensure complete conversion to oxides. The obtained powders were then ground using an alumina mortar and pestle, and subsequently uniaxially pressed at 300 MPa into pellets, with dimensions of ~10 mm in diameter and ~1 mm in thickness.

2.3 Reaction experiments of phase equilibria

In order to completely dissolve TBO during equilibration reaction, CMAS and thermal barrier oxide powders were mixed to achieve a 25 mol.% concentration of the TBO cations (1 mol of cations), e.g. $0.75Ca_{33}Mg_9Al_{13}Si_{45} + 0.25RE_{50}Ta_xZr_{50-x}$. This was done to ensure that there is a residual glass phase after all interactions, in order to record the saturation limit of RE, Ta and Zr in the melt relative to the formation of reaction products such as fluorite and apatite. To ensure a homogeneous mixture, mixed CMAS−TBO powders in an ethanol-based slurry were ground in an agate mortar with a pestle until dry. The mixed powders were then cold pressed into 10 mm-diameter pellets. The pellets in a corundum crucible were annealed for 5500 h at 1300 °C in a box furnace. Specimens were then quenched in the air to room temperature by the rapid withdrawal.

2.4 CMAS penetration experiments

The obtained TBO pellets were ground using 400 and 800 grit SiC abrasive papers, and polished for 10 min. The obtained CMAS powders were put in absolute alcohol and fully stirred. Subsequently, the slurry was dropped on the $RE_{50}Ta_xZr_{50-x}$ bulk surfaces with a concentration of about 30 mg/cm^2. After the complete evaporation of ethanol, the samples with homogeneous CMAS deposits were obtained. All the samples were heat-treated in a box electric furnace at 1300 °C for 4 h.

2.5 Characterization

The microstructural characterization of penetration experimental and equilibrated specimens was carried out using a JSM−7500F field emission scanning electron microscope (FE-SEM) equipped with a backscattered electron (BSE) detector, and the elemental compositions were measured using the energy dispersive X-ray spectroscopy (EDS) in the SEM and the wavelength dispersive spectroscopy (WDS) in an electron probe micro-analyser (EPMA) (JXA−8530, JEOL, Japan). The measurements were taken from 3 individual grains for each phase. The phase constitutions of the sample were determined by means of X-ray diffraction (XRD) at ambient temperature and analyzed on X-ray diffractometer (D8-advance, Bruker, Germany) with a Cu K_α radiation at 40 kV and 40 mA. The XRD pattern was acquired in the 2θ range from 10° to 90° with data collected by a step of 0.02°.

3 Results

The reaction product identities in this work are listed in Table 1. The XRD patterns and microstructures resulting from chemical reactions between various TBO and molten CMAS at 1300 °C for 50 h are presented in Fig. 1 and Figs. 2−5, respectively. The equilibrium phases for each combination after reaction experiments of phase equilibria and the measuring compositions of equilibrium phases are summarized in Tables 2−4, respectively. The cross-sectional SEM micrographs of $RE_{50}Ta_xZr_{50-x}$ oxides after CMAS attack at 1300 °C for 4 h are shown in Figs. 6−9, and the penetration depths of different TBO bulks are listed in Table 5. The detailed results from our experiments are described in the following sections.

3.1 Phase equilibrium of TBO and molten CMAS interactions

Figure 1(a) shows the XRD patterns for $Yb_{50}Ta_xZr_{50-x}$ (x=10, 20, 30, 40) reacted with CMAS, which suggests that equilibrium phases are apatite, fluorite (c-ZrO_2) and M′-$YbTaO_4$ phases. The fluorite phases can be detected in all $Yb_{50}Ta_xZr_{50-x}$ samples, and the residual M′-$YbTaO_4$ phases can be recorded in $Yb_{50}Ta_{30}Zr_{20}$ and $Yb_{50}Ta_{40}Zr_{10}$ samples. The apatite phases formed by interaction with $Yb_{50}Ta_{10}Zr_{40}$ and $Yb_{50}Ta_{20}Zr_{30}$ can be determined, and the XRD peaks of apatite phases rapidly decrease when the $TaO_{2.5}$ content increases. This implies that the addition of Ta^{5+} can decrease the amount of Yb^{3+} available to form apatite, which is consistent with the previous study [17]. The microstructures for $Yb_{50}Ta_xZr_{50-x}$ reacted with CMAS are exhibited in Fig. 2 and the apatite, fluorite and $YbTaO_4$ phases are marked, which is essentially consistent with our XRD results. For $Yb_{50}Ta_{30}Zr_{20}$, very few apatite phases can be observed in the microstructures (Fig. 2(c)), and they cannot be measured by XRD. This is because the amount of apatite phases is below the measurement limit of XRD technology. The compositions of apatite and fluorite were $38.6SiO_2-45.7YbO_{1.5}-14.5CaO-1.2ZrO_2$ and $26.9ZrO_2-39.8YbO_{1.5}-26.1TaO_{2.5}-10.3CaO$ determined by EDS, respectively. For $Yb_{50}Ta_{40}Zr_{10}$, many residual $YbTaO_4$ phases can be observed, which exhibits that the $YbTaO_4$ phases are inactive when reacting with the CMAS melt. The morphologies of fluorite and apatite phases are spherical and needlelike, which is similar to the previous studies [15,17]. By comparing these images of Fig. 2, the sizes of fluorite phases decrease when increasing the content of $TaO_{2.5}$ in

Table 1 Crystalline reaction product identities after TBO + $Ca_{33}Mg_9Al_{13}Si_{45}$ interactions at 1300 °C

Phase	Abbreviation	Nominal formula	Structure	Space group
Fluorite	F	$(Zr, RE, Ta, Ca)O_{1.x}$	Cubic	$Fm\bar{3}m$
Apatite	Ap	$(Ca, RE)_4(RE, Zr)_6(SiO_4)_6O_2$	Hexagonal	$P63/m$
Yttrium(Ytterbium) tantalate	Yb(Y)T	$Y(Yb)TaO_4$	Monoclinic	$P2/a$
Pyrochlore	P	$(Ca,Y)_2(Ta)_2(O_7\square_1)$	Cubic	$Fd\bar{3}m$

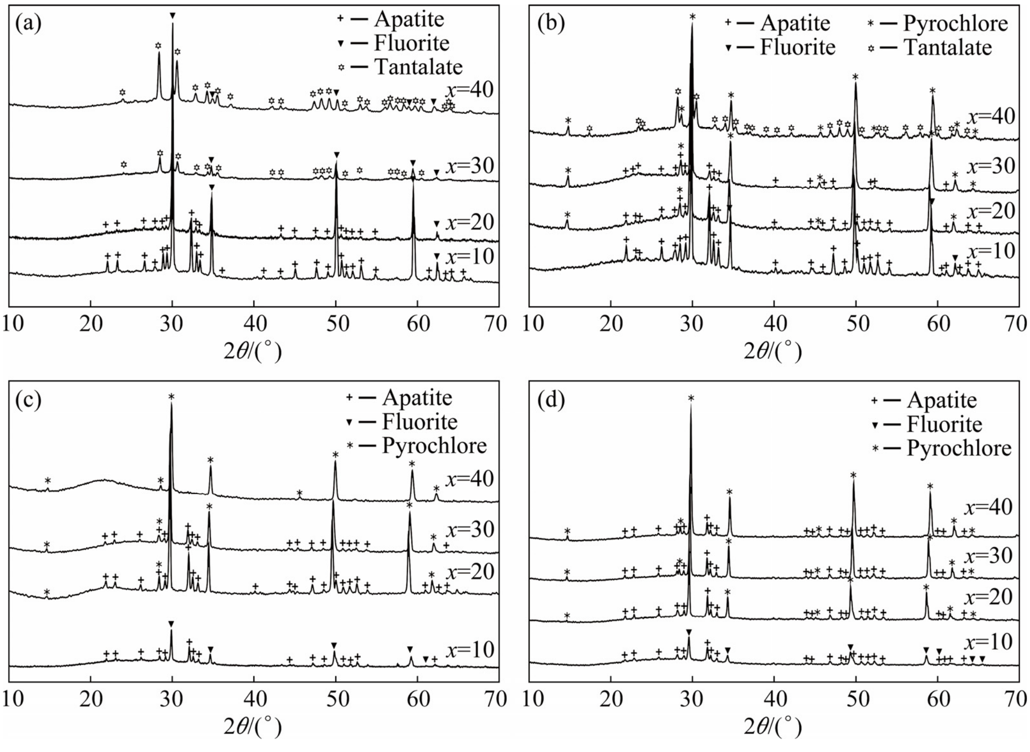

Fig. 1 XRD patterns resulting from chemical reactions between $RE_{50}Ta_xZr_{50-x}$ (RE=Yb, Y, Dy, Gd; x=10, 20, 30, 40) and molten CMAS at 1300 °C for 50 h: (a) $Yb_{50}Ta_xZr_{50-x}$; (b) $Y_{50}Ta_xZr_{50-x}$; (c) $Dy_{50}Ta_xZr_{50-x}$; (d) $Gd_{50}Ta_xZr_{50-x}$

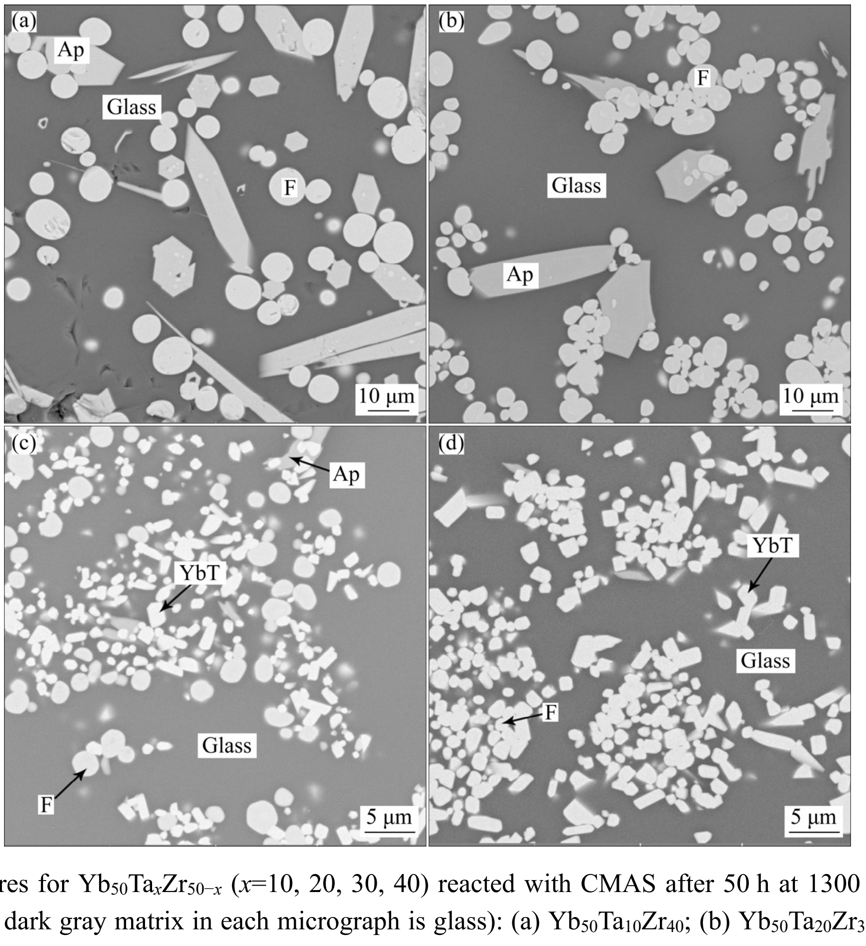

Fig. 2 Microstructures for $Yb_{50}Ta_xZr_{50-x}$ (x=10, 20, 30, 40) reacted with CMAS after 50 h at 1300 °C with increasing $TaO_{2.5}$ content (The dark gray matrix in each micrograph is glass): (a) $Yb_{50}Ta_{10}Zr_{40}$; (b) $Yb_{50}Ta_{20}Zr_{30}$; (c) $Yb_{50}Ta_{30}Zr_{20}$; (d) $Yb_{50}Ta_{40}Zr_{10}$

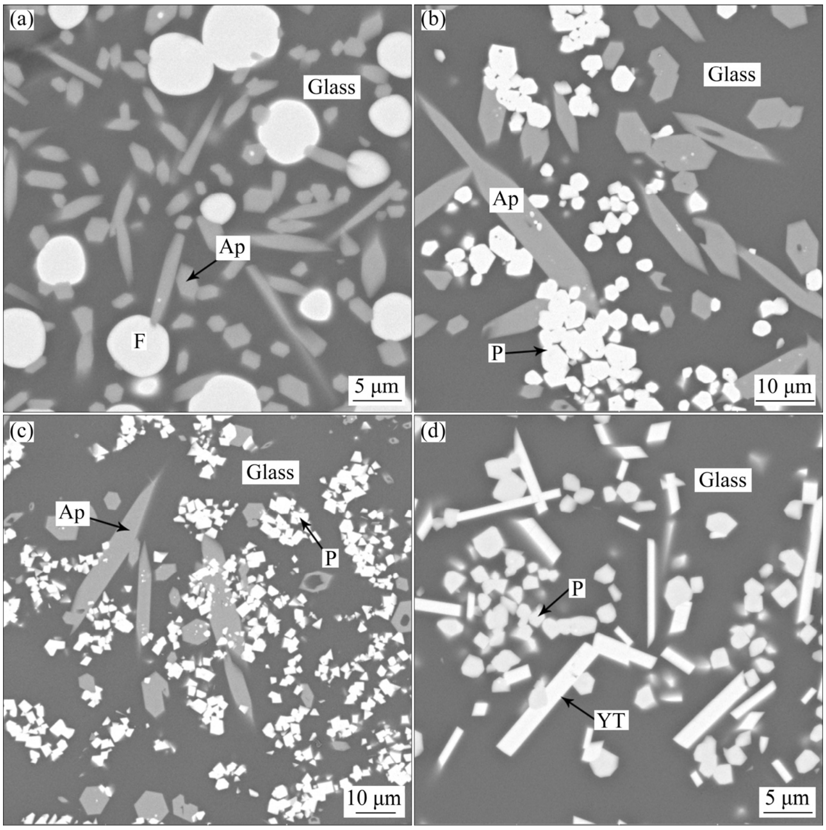

Fig. 3 Microstructures for $Y_{50}Ta_{x}Zr_{50-x}$ (x=10, 20, 30, 40) reacted with CMAS after 50 h at 1300 °C with increasing $TaO_{2.5}$ content (The dark gray matrix in each micrograph is glass): (a) $Y_{50}Ta_{10}Zr_{40}$; (b) $Y_{50}Ta_{20}Zr_{30}$; (c) $Y_{50}Ta_{30}Zr_{20}$; (d) $Y_{50}Ta_{40}Zr_{10}$

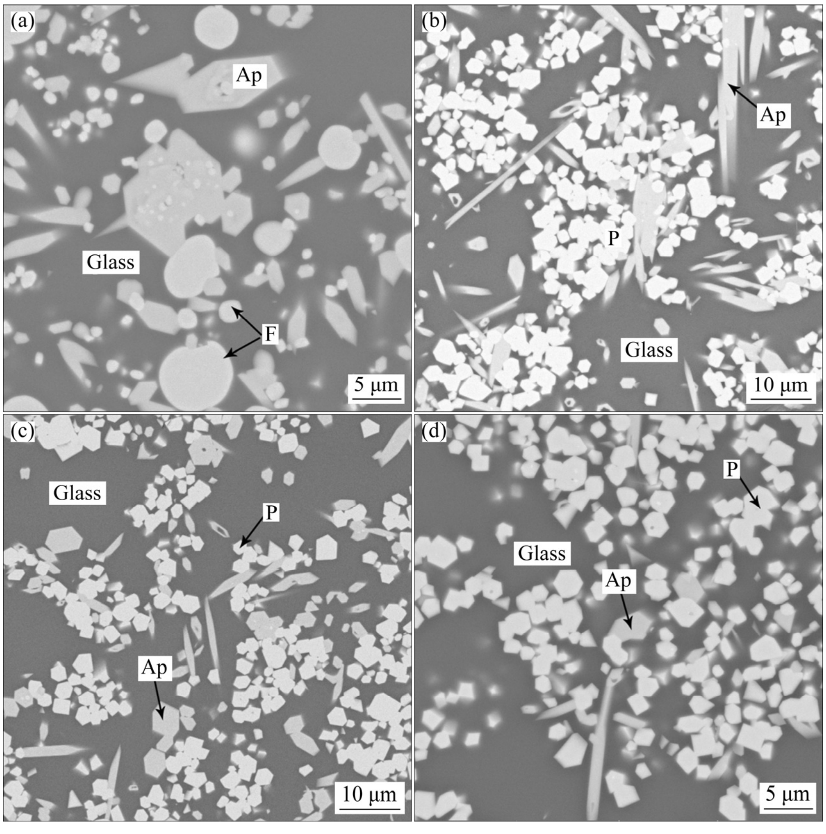

Fig. 4 Microstructures for $Dy_{50}Ta_{x}Zr_{50-x}$ (x=10, 20, 30, 40) reacted with CMAS after 50 h at 1300 °C with increasing $TaO_{2.5}$ content (The dark gray matrix in each micrograph is glass): (a) $Dy_{50}Ta_{10}Zr_{40}$; (b) $Dy_{50}Ta_{20}Zr_{30}$; (c) $Dy_{50}Ta_{30}Zr_{20}$; (d) $Dy_{50}Ta_{40}Zr_{10}$

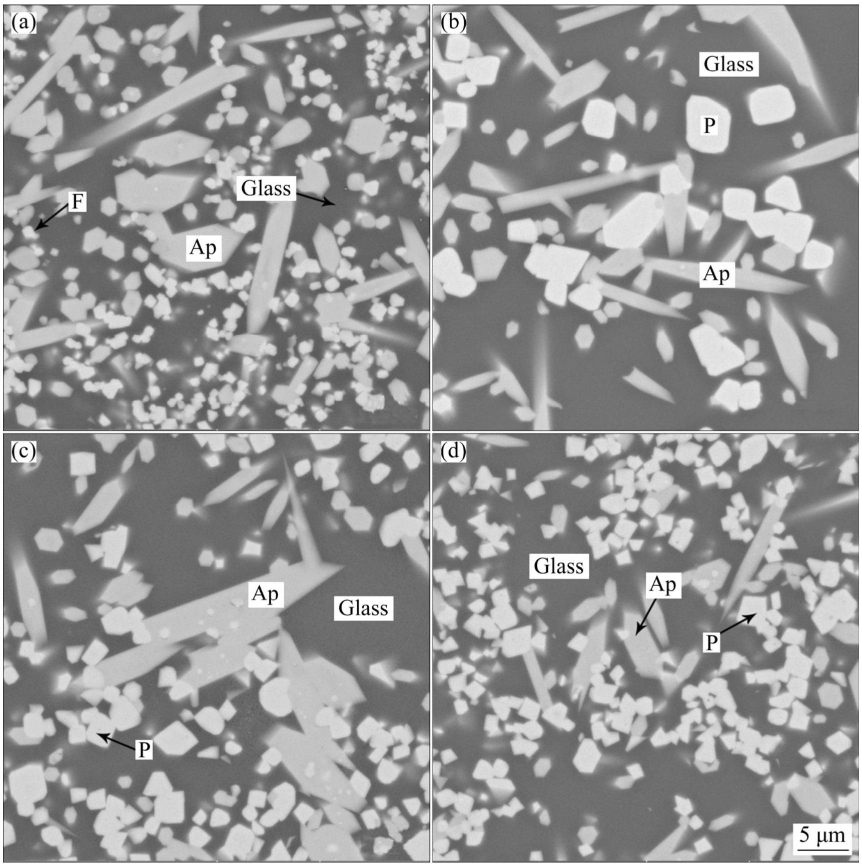

Fig. 5 Microstructures for $Gd_{50}Ta_{x}Zr_{50-x}$ (x=10, 20, 30, 40) reacted with CMAS after 50 h at 1300 °C with increasing $TaO_{2.5}$ content (The dark gray matrix in each micrograph is glass): (a) $Gd_{50}Ta_{10}Zr_{40}$; (b) $Gd_{50}Ta_{20}Zr_{30}$; (c) $Gd_{50}Ta_{30}Zr_{20}$; (d) $Gd_{50}Ta_{40}Zr_{10}$

Table 2 Observed equilibrium phases in TBO and $Ca_{33}Mg_{9}Al_{13}Si_{45}$ reactions at 1300 °C for 50 h

TBO	Reaction product[a]	TBO	Reaction product[a]
$Yb_{50}Ta_{10}Zr_{40}$	Liq.+Ap+F	$Y_{50}Ta_{10}Zr_{40}$	Liq.+Ap+F
$Yb_{50}Ta_{20}Zr_{30}$	Liq.+Ap+F	$Y_{50}Ta_{20}Zr_{30}$	Liq.+Ap+P
$Yb_{50}Ta_{30}Zr_{20}$	Liq.+Ap+F+YbT	$Y_{50}Ta_{30}Zr_{20}$	Liq.+Ap+P
$Yb_{50}Ta_{40}Zr_{10}$	Liq.+F+YbT	$Y_{50}Ta_{40}Zr_{10}$	Liq.+YT+P
$Dy_{50}Ta_{10}Zr_{40}$	Liq.+Ap+F	$Gd_{50}Ta_{10}Zr_{40}$	Liq.+Ap+F
$Dy_{50}Ta_{20}Zr_{30}$	Liq.+Ap+P	$Gd_{50}Ta_{20}Zr_{30}$	Liq.+Ap+P
$Dy_{50}Ta_{30}Zr_{20}$	Liq.+Ap+P	$Gd_{50}Ta_{30}Zr_{20}$	Liq.+Ap+P
$Dy_{50}Ta_{40}Zr_{10}$	Liq.+Ap+P	$Gd_{50}Ta_{40}Zr_{10}$	Liq.+Ap+P

[a] Phase identification was based on measured compositions, phase morphology and XRD patterns

$Yb_{50}Ta_{x}Zr_{50-x}$, and the fluorite phases with coarse and fine grains can be observed in Fig. 2(c) ($Yb_{50}Ta_{30}Zr_{20}$). The various sizes of fluorite phases may significantly affect the CMAS penetration.

Figures 1(b) and 3 show the XRD patterns and microstructures for $Y_{50}Ta_{x}Zr_{50-x}$ (x=10, 20, 30, 40) reacted with CMAS. The equilibrium phases for each combination are summarized in Table 2, and the apatite, fluorite, pyrochlore and $YTaO_4$ phases can be recorded. In comparison with the $Yb_{50}Ta_{x}Zr_{50-x}$, the pyrochlore phases rather than fluorite phases were determined in $Y_{50}Ta_{20}Zr_{30}$, $Y_{50}Ta_{30}Zr_{20}$ and $Y_{50}Ta_{40}Zr_{10}$. The XRD patterns of pyrochlore ($Fd\overline{3}m$) and fluorite ($Fm\overline{3}m$) phases are similar, and a additional diffraction peak (2θ) between 14° and 16° was used to distinguish

Table 3 Measured chemical compositions of major phases after TBO + $Ca_{33}Mg_{9}Al_{13}Si_{45}$ reactions (mol.%)

TBO	Apatite[a]				Fluorite				Pyrochlore[b]			
	Si	RE	Ca	Zr	Zr	RE	Ta	Ca	Ca	RE	Ta	Zr
$Yb_{50}Ta_{10}Zr_{40}$	38.3	44.4	15.0	2.3	44.7[a]	37.4[a]	14.5[a]	3.4[a]	−	−	−	−
$Yb_{50}Ta_{20}Zr_{30}$	37.9	45.7	14.4	2.0	28.4[a]	39.0[a]	24.6[a]	8.0[a]	−	−	−	−
$Yb_{50}Ta_{30}Zr_{20}$	38.6	45.7	14.5	1.2	26.9[a]	39.8[a]	26.1[a]	10.3[a]	−	−	−	−
$Y_{50}Ta_{10}Zr_{40}$	39.0	45.8	14.5	0.7	46.9[b]	32.2[b]	13.8[b]	7.1[b]	−	−	−	−
$Y_{50}Ta_{20}Zr_{30}$	38.6	46.2	14.5	0.6	−	−	−	−	15.3	34.6	27.4	22.7
$Y_{50}Ta_{30}Zr_{20}$	39.1	46.2	14.2	0.5	−	−	−	−	18.5	32.6	39.5	9.4
$Y_{50}Ta_{40}Zr_{10}$	−	−	−	−	−	−	−	−	25.7	28.6	42.5	3.2
$Dy_{50}Ta_{10}Zr_{40}$	37.6	44.3	15.2	2.9	43.6[b]	28.9[b]	15.2[b]	12.3[b]	−	−	−	−
$Dy_{50}Ta_{20}Zr_{30}$	37.7	44.9	14.9	2.4	−	−	−	−	14.8	34.7	25.5	25.0
$Dy_{50}Ta_{30}Zr_{20}$	37.4	47.3	13.8	1.6	−	−	−	−	18.4	30.1	36.4	15.1
$Dy_{50}Ta_{40}Zr_{10}$	37.5	46.9	14.5	1.1	−	−	−	−	21.0	31.0	40.1	7.9
$Gd_{50}Ta_{10}Zr_{40}$	36.9	45.2	14.9	3.0	39.1[b]	27.7[b]	15.1[b]	18.1[b]	−	−	−	−
$Gd_{50}Ta_{20}Zr_{30}$	37.1	46.8	13.8	2.3	−	−	−	−	18.9	29.7	31.2	20.2
$Gd_{50}Ta_{30}Zr_{20}$	36.8	48.1	13.6	1.5	−	−	−	−	21.2	30.8	36.6	11.4
$Gd_{50}Ta_{40}Zr_{10}$	37.4	48.0	13.7	0.9	−	−	−	−	25.6	29.0	42.8	2.6

[a] Reaction product compositions determined by EPMA−WDS; [b] Measured compositions via SEM−EDS

Table 4 Compositions of YbT and YT measured via SEM−EDS (mol.%)

System	Ca	RE	Ta	Zr
$Yb_{50}Ta_{30}Zr_{20}$+$Ca_{33}Mg_{9}Al_{13}Si_{45}$	2.5	44.3	48.3	4.9
$Yb_{50}Ta_{40}Zr_{10}$+$Ca_{33}Mg_{9}Al_{13}Si_{45}$	2.3	43.9	49.6	4.2
$Y_{50}Ta_{40}Zr_{10}$+$Ca_{33}Mg_{9}Al_{13}Si_{45}$	2.4	45.3	52.3	0.0

these two phases [32]. The morphologies of these two phases are also different, fluorite phases are spherical and pyrochlore phases are angular. Besides, the pyrochlore phases prefer to get together and the fluorite phases prefer to disperse. The apatite phases are formed in $Y_{50}Ta_{10}Zr_{40}$, $Y_{50}Ta_{20}Zr_{30}$ and $Y_{50}Ta_{30}Zr_{20}$. The amount of apatite phases gradually decreases from $Y_{50}Ta_{10}Zr_{40}$ to $Y_{50}Ta_{30}Zr_{20}$, which implies that increasing the $TaO_{2.5}$ content can reduce the effective Y^{3+} to generate apatite phases. The residual $YTaO_4$ phases can be found in $Y_{50}Ta_{40}Zr_{10}$, but residual $YbTaO_4$ phases can be recorded at low $TaO_{2.5}$ content ($Yb_{50}Ta_{30}Zr_{20}$).

Figures 1(c, d), 4 and 5 show the XRD patterns and microstructures of $Dy_{50}Ta_{x}Zr_{50-x}$ and $Gd_{50}Ta_{x}Zr_{50-x}$ (x=10, 20, 30, 40) reacted with CMAS, respectively. The results of these two systems are similar, and the equilibrium phases after chemical reactions for each combination are summarized in Table 2. With increasing the content of $TaO_{2.5}$, the amount of apatite phases decreases, and the reaction products switch from reprecipitated fluorite phases to pyrochlore phases. The apatite phases can be formed in Dy(Gd)$_{50}Ta_{40}Zr_{10}$ with the highest content of $TaO_{2.5}$, which is not determined in Yb(Y)$_{50}Ta_{40}Zr_{10}$. Besides, the amount of apatite phases is higher in $Gd_{50}Ta_{40}Zr_{10}$ than that in $Dy_{50}Ta_{40}Zr_{10}$. From Gd^{3+} to Yb^{3+}, the ionic size of the RE cation decreases and our experiments show that the amount of apatite phase decreases. This means that the formation ability of the apatite phase is proportional to the ionic size of the RE cation in $RE_{50}Ta_{x}Zr_{50-x}$ systems, which is consistent with previous studies [16].

The compositions of apatite phases in various $RE_{50}Ta_{x}Zr_{50-x}$ systems are listed in Table 3, which is not significantly altered. The content of SiO_2 is in a reasonable range from 36.8 to 39.1 mol.%, which is expected to be 37.5 mol.% for general formula $Ca_2RE_8(SiO_4)_6O_2$. The contents of CaO and $REO_{1.5}$ in various samples are in the range from 13.6 to 15.2 mol.% and from 44.3 to 48.1 mol.%, respectively. Besides, a trace of ZrO_2 can be detected

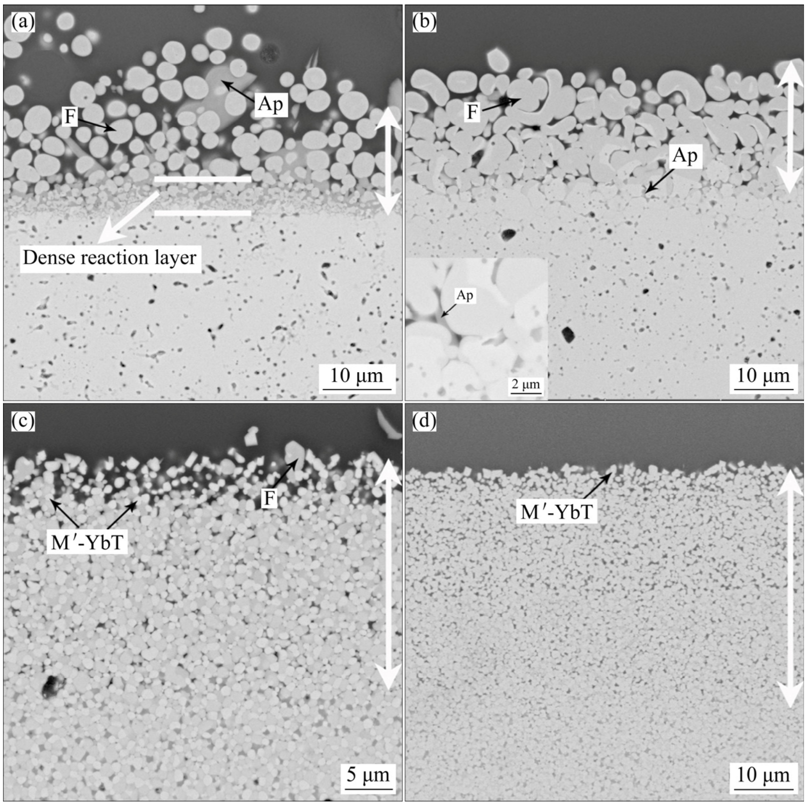

Fig. 6 Cross-section SEM images of CMAS-attacked $Yb_{50}Ta_xZr_{50-x}$ (x=10, 20, 30, 40) bulks at 1300 °C for 4 h with increasing $TaO_{2.5}$ content (The dark gray matrix above reaction layer in each micrograph is the residual CMAS): (a) $Yb_{50}Ta_{10}Zr_{40}$; (b) $Yb_{50}Ta_{20}Zr_{30}$; (c) $Yb_{50}Ta_{30}Zr_{20}$; (d) $Yb_{50}Ta_{40}Zr_{10}$

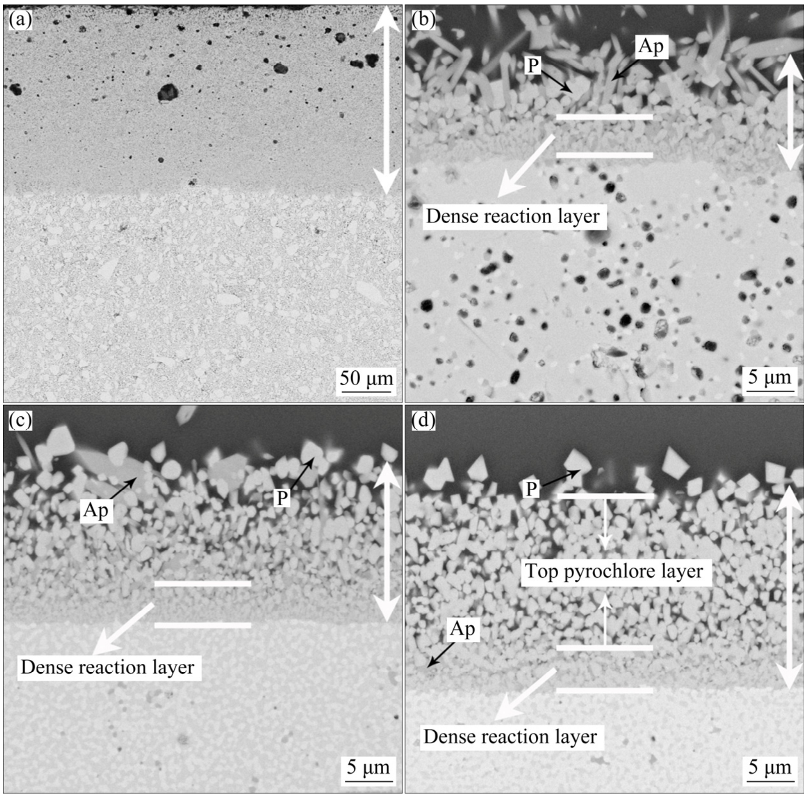

Fig. 7 Cross-section SEM images of CMAS-attacked $Y_{50}Ta_xZr_{50-x}$ (x=10, 20, 30, 40) bulks at 1300 °C for 4 h with increasing $TaO_{2.5}$ content (The dark gray matrix above reaction layer in each micrograph is the residual CMAS, and the parts at the bottom left-hand corner are the enlarged images): (a) $Y_{50}Ta_{10}Zr_{40}$; (b) $Y_{50}Ta_{20}Zr_{30}$; (c) $Y_{50}Ta_{30}Zr_{20}$; (d) $Y_{50}Ta_{40}Zr_{10}$

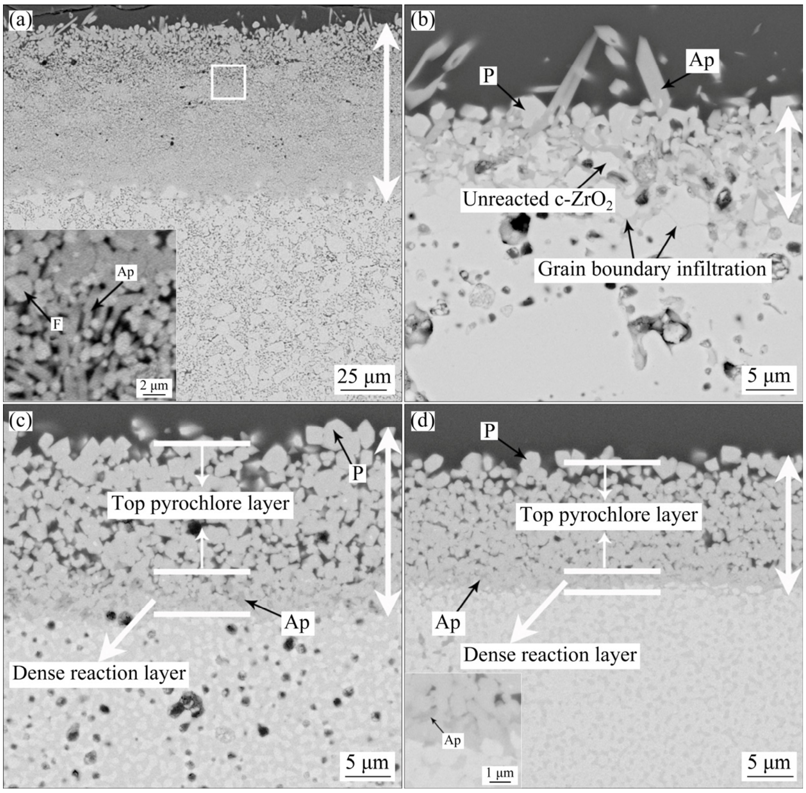

Fig. 8 Cross-section SEM images of CMAS-attacked $Dy_{50}Ta_xZr_{50-x}$ (x=10, 20, 30, 40) bulks at 1300 °C for 4 h with increasing $TaO_{2.5}$ content (The dark gray matrix above reaction layer in each micrograph is the residual CMAS, and the parts at the bottom left-hand corner are the enlarged images): (a) $Dy_{50}Ta_{10}Zr_{40}$; (b) $Dy_{50}Ta_{20}Zr_{30}$; (c) $Dy_{50}Ta_{30}Zr_{20}$; (d) $Dy_{50}Ta_{40}Zr_{10}$

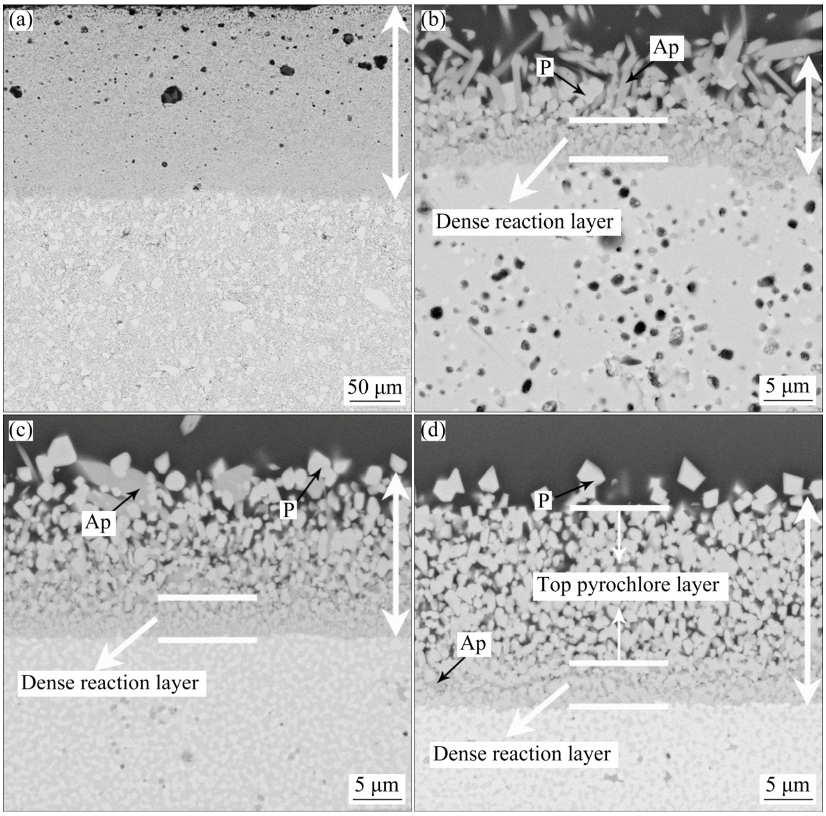

Fig. 9 Cross-section SEM images of CMAS-attacked $Gd_{50}Ta_xZr_{50-x}$ (x=10, 20, 30, 40) bulks at 1300 °C for 4 h with increasing $TaO_{2.5}$ content (The dark gray matrix above reaction layer in each micrograph is the residual CMAS): (a) $Gd_{50}Ta_{10}Zr_{40}$; (b) $Gd_{50}Ta_{20}Zr_{30}$; (c) $Gd_{50}Ta_{30}Zr_{20}$; (d) $Gd_{50}Ta_{40}Zr_{10}$

Table 5 Measured penetration depths in TBO and $Ca_{33}Mg_9Al_{13}Si_{45}$ reactions at 1300 °C for 4 h

TBO	Penetration depth/μm	TBO	Penetration depth/μm	TBO	Penetration depth/μm	TBO	Penetration depth/μm
$Yb_{50}Ta_{10}Zr_{40}$	19±3	$Y_{50}Ta_{10}Zr_{40}$	174±5	$Dy_{50}Ta_{10}Zr_{40}$	85±3	$Gd_{50}Ta_{10}Zr_{40}$	195±10
$Yb_{50}Ta_{20}Zr_{30}$	21±2	$Y_{50}Ta_{20}Zr_{30}$	9±2	$Dy_{50}Ta_{20}Zr_{30}$	12±2	$Gd_{50}Ta_{20}Zr_{30}$	13±2
$Yb_{50}Ta_{30}Zr_{20}$	26±2	$Y_{50}Ta_{30}Zr_{20}$	22±3	$Dy_{50}Ta_{30}Zr_{20}$	19±2	$Gd_{50}Ta_{30}Zr_{20}$	18±2
$Yb_{50}Ta_{40}Zr_{10}$	38±2	$Y_{50}Ta_{40}Zr_{10}$	38±2	$Dy_{50}Ta_{40}Zr_{10}$	13±2	$Gd_{50}Ta_{40}Zr_{10}$	22±2

in the apatite phases. The compositions of fluorite and pyrochlore phases are listed in Table 3. For samples $Yb_{50}Ta_xZr_{50-x}$, the capture of Yb^{3+} by the reprecipitated fluorite slightly increases from 37.4% to 39.8%. Contents of CaO and $TaO_{2.5}$ in the reprecipitated fluorite increase from 3.4 to 10.3 mol.% and from 14.5 to 26.1 mol.%, respectively. The ZrO_2 content decreases from 44.7 to 26.9 mol.%. For pyrochlore phases, the content of ZrO_2 decreases and that of CaO increases when increasing the $TaO_{2.5}$ content in $RE_{50}Ta_xZr_{50-x}$ (RE=Y, Dy, Gd; x=20, 30, 40). The measured compositions exhibit that pyrochlore phases have a large solid solubility. Based on the experimental compositions, increasing $TaO_{2.5}$ content in $RE_{50}Ta_xZr_{50-x}$ can result in increasing the contents of $TaO_{2.5}$ and CaO in both fluorite and pyrochlore phases. Table 4 exhibits the compositions of the residual Yb(Y)T phases, which shows that some CaO can be detected after reaction experiments of phase equilibria.

3.2 CMAS resistance of $RE_{50}Ta_xZr_{50-x}$ bulks

The sintered $RE_{50}Ta_xZr_{50-x}$ pellets were used to carry out CMAS penetration experiments in order to understand their resistance to CMAS corrosion. CMAS powders were deposited on the surfaces of $RE_{50}Ta_xZr_{50-x}$ bulks, and then the samples covered by CMAS were annealed at 1300 °C for 4 h. Figures 6−9 show cross-sectional SEM micrographs of $RE_{50}Ta_xZr_{50-x}$ oxides after CMAS attack. The penetration depths of various TBO bulks after CMAS attack at 1300 °C for 4 h are shown in Table 5 and Fig. 10.

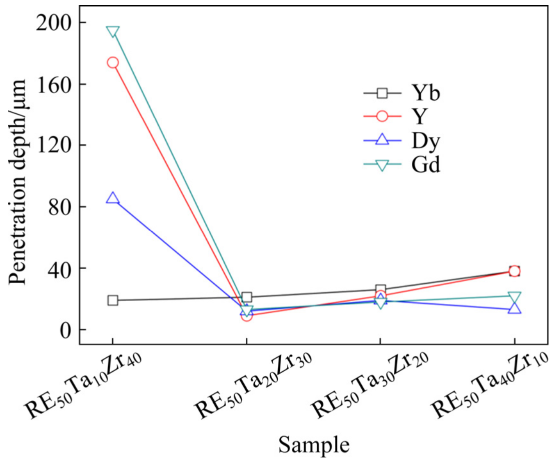

Fig. 10 Measured penetration depths in TBO ($RE_{50}Ta_xZr_{50-x}$) and $Ca_{33}Mg_9Al_{13}Si_{45}$ reactions at 1300 °C for 4 h

The cross-sectional microstructures of $Yb_{50}Ta_xZr_{50-x}$ after CMAS penetration are shown in Figs. 6(a−d). Phase equilibrium experiments show that apatite phases can form after chemical reactions of $Yb_{50}Ta_xZr_{50-x}$ (x=10, 20, 30) and CMAS. However, during the CMAS infiltration the apatite phases can only be easily observed in sample $Yb_{50}Ta_{10}Zr_{40}$ as shown in Fig. 6(a). In this figure, coarse and spherical reprecipitation fluorite phases (c-ZrO_2) and needlelike apatite phases can be easily seen near the surface, and their morphologies are similar with those in phase equilibrium experiment. At the interface between corroded and uncorroded areas, many fine and needlelike apatite phases are produced, and then a dense reaction layer is generated. The dense layer can seal CMAS infiltration channels and limit the infiltrated layer thickness to be about 10 μm. For the $Yb_{50}Ta_{20}Zr_{30}$ sample in Fig. 6(b), coarse reprecipitation fluorite phases can be observed after CMAS penetration, but no coarse apatite phases can be found though they can easily form in the phase equilibrium experiment (Fig. 2(b)). Some fine apatite phases can be observed in the bottom left enlarged image, but they are rare and no dense reaction layer can be generated near the reaction front. Therefore, the CMAS penetration should not be blocked. However, it is surprising that the infiltrated depth is about 21 μm for $Yb_{50}Ta_{20}Zr_{30}$. For sample $Yb_{50}Ta_{30}Zr_{20}$, its composition is located in the two-phase region of ternary phase diagram, and the tantalate phase (M′-$YbTaO_4$) is coexistent with the fluorite phase as shown at the bottom of Fig. 6(c). As discussed in Fig. 2(c), $YbTaO_4$ is not active when reacting with the CMAS melt and very few apatite phases can be formed, which is confirmed by the penetration experiment. After CAMS infiltration in Fig. 6(c), grey reprecipitation fluorite phases can be produced, and many micropores are generated along with corrosion reactions. These micropores can be used to distinguish corroded and uncorroded areas. The white phases are $YbTaO_4$, and they are evenly distributed in the sample from top to bottom. Moreover, their morphologies are similar compared with the corroded and uncorroded areas. The apatite phase can be found in Fig. 6(c) as pointed by arrows. Its amount is very few and a dense reaction layer cannot be formed. The infiltrated layer thickness of this sample is about 26 μm. For $Yb_{50}Ta_{40}Zr_{10}$ sample after CMAS attack, its infiltrated feature is similar to that of $Yb_{50}Ta_{30}Zr_{20}$ sample, and the difference is that the amount of $YbTaO_4$ increases and no coarse reprecipitation fluorite phase can be generated. As shown in Fig. 6(d), the penetration depth is about 38 μm, which is the largest among these $Yb_{50}Ta_xZr_{50-x}$ samples.

Penetration experiments between CMAS and $Y_{50}Ta_xZr_{50-x}$ samples are illustrated in Figs. 7(a−d). Figure 7(a) exhibits the cross-sectional microstructures of $Y_{50}Ta_{10}Zr_{40}$ after CMAS penetration. Many reprecipitated fluorite and needle-like apatite phases can be observed in the sample. Unlike the experimental results in Fig. 6(a), these phases are not coarse as displayed in the enlarged figure and can be observed not only at the interface but also far from the interface. The corrosion microstructure of $Y_{50}Ta_{10}Zr_{40}$ exhibits that the apatite phases are difficult to coarsen during CMAS attack. Another feature of the corroded $Y_{50}Ta_{10}Zr_{40}$ sample is that many pores can be observed above the interface. The appearance and growth of pores in the residual melt are found and discussed in previous literature [33]. The formation of pores suggests that gas enters the melt during the infiltrated process. The movement of gas bubbles toward the surface is partially responsible for the distribution of apatite and reprecipitated fluorite throughout the residual CMAS melt in Fig. 7(a). The infiltrated thickness for the $Y_{50}Ta_{10}Zr_{40}$ sample is about 174 μm. Because the movement of gas bubbles can lead to the movement of reaction products, the real infiltrated thickness should be much smaller than 174 μm. The reaction layer cannot seal infiltration channels during CMAS attack and no dense layer can be formed. For $Y_{50}Ta_{20}Zr_{30}$ sample in Fig. 7(b), the cross-sectional microstructures show that its penetration depth is about 9 μm and a dense reaction layer can be generated. Some dispersive apatite phases can be observed near the reaction layer. During CMAS penetration, the formation of apatite and pyrochlore as measured in Fig. 3(b) is confirmed. Fine apatite and pyrochlore phases are tightly bound together at the reaction front, which can block CMAS infiltration channels. By comparing the corrosion microstructure of $Y_{50}Ta_{10}Zr_{40}$ with $Y_{50}Ta_{20}Zr_{30}$, the mixture of apatite and fluorite phases in Fig. 7(a) cannot generate a dense layer, but the dense layer can be formed through the mixture of apatite and pyrochlore phases. This phenomenon may be derived from different morphologies of fluorite and pyrochlore phases. The angular and polygonal pyrochlore phase is easy to combine with the needlelike apatite phase, but the spherical fluorite phase is not effective. For the $Y_{50}Ta_{30}Zr_{20}$ sample in Fig. 7(c), its composition is located in the two-phase region of ternary phase diagram, and white tantalate phases ($YTaO_4$) are existent. Even so, reaction products during CMAS attack are still apatite and pyrochlore phases, and its infiltrated feature is similar to that of the $Y_{50}Ta_{30}Zr_{20}$ pellet. Its penetration depth is about 22 μm, which is a little larger than that of $Y_{50}Ta_{20}Zr_{30}$ because less amount of apatite is produced. Figure 7(d) exhibits the cross-sectional microstructures of $Y_{50}Ta_{40}Zr_{10}$ after CMAS penetration. The total infiltrated thickness is about 38 μm, and three different corrosion layers can be easily distinguished. In the top corrosion layer, the main reaction products are the pyrochlore phases, the middle layer contain pyrochlore and some unreacted tantalate phases, and the bottom corrosion layer contains pyrochlore (grey), apatite (black) and tantalate (white) phases. The varying morphologies along with the infiltrated depth are possible to be related with the amount of molten CMAS. At the top, the amount of CMAS is sufficient to react with thermal barrier oxides, and all oxides are transformed to be pyrochlore phase. As penetration goes on, the amount of CMAS decreases and is not sufficient to make all oxides transform to pyrochlore phase, and some unreacted tantalate phases are left. As the amount of CMAS continues to decrease, more unreacted tantalate phases are residual and some apatite phases are formed. Due to the existence of unreacted tantalate phase, apatite and pyrochlore phases cannot be tightly bound together, and the dense layer cannot be formed.

Figures 8(a−d) exhibit the cross-sectional microstructures of $Dy_{50}Ta_xZr_{50-x}$ systems after CMAS penetration. In Fig. 8(a) and the enlarged picture, many needlelike apatite and spherical reprecipitation fluorite phases can be observed. At the top of reaction layer, some coarse fluorites can be found. However, their sizes become small along the infiltrated direction, and no dense layer is generated. Therefore, CMAS infiltration is not blocked and its penetration depth is very large (about 85 μm). For $Dy_{50}Ta_{20}Zr_{30}$ in Fig. 8(b), needlelike apatite and polygonal pyrochlore phases can be observed after CMAS penetration. The penetration depth is about 12 μm, and a dense reaction layer seems to be formed. However, an interesting phenomenon can be seen in the sample. Corrosion reactions go on through the grain boundary as pointed by arrows in Fig. 8(b), and some unreacted fluorite phases are surrounded by reaction products. Corrosion behavior through grain boundary is detrimental to resist CMAS penetration. For $Dy_{50}Ta_{30}Zr_{20}$ and $Dy_{50}Ta_{40}Zr_{10}$ samples, their compositions are both located in the two-phase region of ternary phase diagram, and their corroded microstructures are similar, as shown in Figs. 8(c) and (d). The dense reaction layers near the reaction front are generated in these two samples after CMAS penetration. It is worth mentioning that the top pyrochlore layers can be observed in these two systems. The infiltration thickness of $Dy_{50}Ta_{30}Zr_{20}$ (19 μm) is a little larger than that of $Dy_{50}Ta_{40}Zr_{10}$ (13 μm) because more pyrochlore phases are precipitated in $Dy_{50}Ta_{40}Zr_{10}$ samples.

The cross-sectional microstructures of $Gd_{50}Ta_xZr_{50-x}$ systems after CMAS penetration are shown in Figs. 9(a−d). For $Gd_{50}Ta_{10}Zr_{40}$ in Fig. 9(a), the characteristic of corrosion microstructure is similar to those in Figs. 7(a) and 8(a). Fine apatite and reprecipitation fluorite phases have no effect on restricting CMAS penetration. Therefore, its infiltrated depth is very large (about 195 μm). Figure 9(b) shows the corrosion microstructure of $Gd_{50}Ta_{20}Zr_{30}$ sample, and a lot of apatite and pyrochlore phases can be found. Moreover, they bind together near the reaction front and a dense reaction layer is formed. The CMAS infiltration is blocked and its penetration depth is about 13 μm. Some white phases (M-$GdTaO_4$) can be observed in the uncorroded region, which means that the solubility of $TaO_{2.5}$ in Gd-based fluorite is lower than those in Yb-, Y- and Dy-based fluorite. It is worth mentioning that a lot of holes derived from sample preparation can be seen from the figure, and they seem to have little influence on the corrosion process. The corrosion microstructure of $Gd_{50}Ta_{30}Zr_{20}$ sample (two-phase region in phase diagram) in Fig. 9(c) is similar to that in Fig. 9(b), and a dense reaction layer is formed. Its penetration depth (about 18 μm) is a little larger than that of $Gd_{50}Ta_{20}Zr_{30}$ (about 13 μm), which may be related with less formation of apatite phase. For the $Gd_{50}Ta_{40}Zr_{10}$ sample in Fig. 9(d), two different corrosion microstructures can be distinguished. The top reaction layer is bare of apatite phases, but near the reaction front apatite and pyrochlore phases bind together and generate a dense reaction layer. Because the morphology of the top pyrochlore layer is porous and it has no effect on resistance to CMAS penetration, its infiltrated depth is about 22 μm.

4 Discussion

Topics of further discussion based on the experimental findings include: (1) the effect of $TaO_{2.5}$ addition and various $REO_{1.5}$ on chemical interactions and reactive crystallization with the model CMAS melt; (2) the ability of c-ZrO_2+$RETaO_4$ two-phase field to mitigate the CMAS infiltration; (3) the comparison of the interaction experiments and CMAS penetration experiments; (4) the resistance to CMAS corrosion in $RE_{50}Ta_x$-Zr_{50-x} systems.

4.1 Effect of $TaO_{2.5}$ addition and various $REO_{1.5}$ on reaction products and reaction mechanism

The examination of the observed equilibrium phases in Table 2 reveals that the main reaction products between molten CMAS and different TBO compositions are apatite, pyrochlore and reprecipitated fluorite phases. Besides, residual tantalate phases can be measured in Ta-rich $Yb_{50}Ta_xZr_{50-x}$ and $Y_{50}Ta_xZr_{50-x}$ systems. The microstructures of chemical reactions between various TBOs and the molten CMAS are listed Figs. 2−5. Based on these figures, some salient findings can be concluded. The first is that the addition of $TaO_{2.5}$ in $RE_{50}Ta_xZr_{50-x}$ systems can reduce the formation of apatite phase and then increase the amount of pyrochlore or fluorite phase, which is consistent with the reported experimental results by ABDUL-JABBAR et al [17]. As discussed in the literature [16], the needlelike apatite phase is effective to seal the CMAS infiltration channels and is considered to be an important reaction phase. The reduction of apatite formation and increase of pyrochlore can significantly affect the CMAS penetration process. The reduction of apatite formation is mainly ascribed to increasing the capture of RE^{3+} by the reprecipitated fluorite or pyrochlore when adding Ta^{5+} into $RE_{50}Ta_xZr_{50-x}$ systems. As listed in Table 3, the Ta^{5+} cation only takes part in nucleation of reprecipitated fluorite or pyrochlore phase, but RE^{3+} takes part in nucleation of all phases. This implies that increasing Ta^{5+} amount in $RE_{50}Ta_xZr_{50-x}$ systems will decrease the amount of RE^{3+} available to form apatite and eventually suppress its formation at Ta-rich samples as shown in Figs. 2(d) and 3(d). The second finding is that the reactive crystallization is reprecipitated fluorite at Ta-lean samples and pyrochlore at Ta-rich samples except $Yb_{50}Ta_xZr_{50-x}$ systems. The morphologies of pyrochlore and reprecipitated fluorite phases are polygonal and spherical, respectively. The polygonal pyrochlore is responsible for generating a dense reaction layer, and this is helpful for restricting CMAS penetration. The third finding is that the formation abilities of apatite and pyrochlore phases are proportional to the ionic radius of RE^{3+} ($Gd^{3+}>Dy^{3+}>Y^{3+}>Yb^{3+}$). Large ionic radius of RE^{3+} can result in formation of apatite and pyrochlore phases, but small RE^{3+} (Yb^{3+} and Y^{3+}) can suppress formation of apatite (Figs. 2(d) and 3(d)) and pyrochlore (Figs. 2(b−d)). Therefore, decreasing the RE^{3+} ionic radius and increasing $TaO_{2.5}$ addition can significantly limit chemical reaction between CMAS and TBOs. This can even make $Yb(Y)TaO_4$ inactive during CMAS infiltration, and then some residual tantalate phases can be existent, as shown in Figs. 2(d) and 3(d). The forth one is that the ionic radius of RE^{3+} can affect the morphologies of reaction products. For small Yb^{3+} and Y^{3+}, the size of the fluorite phase is large, as shown in Figs. 2(a) and 3(a). For larger Dy^{3+}, small and large fluorite phases can both be observed in Fig. 4(a), and only small fluorite phase can be measured in Fig. 5(a) for the largest Gd^{3+}.

4.2 Ability of c-ZrO_2 + $RETaO_4$ two-phase field to mitigate CMAS infiltration

As explained in Section 1, RE-rich TBOs can provide sufficient $REO_{1.5}$ to ensure reactive crystallization of apatite phase in order to resist CMAS penetration. However, RE-rich compositions are usually located in the fluorite (c-ZrO_2) phase field, and they exhibit inadequate toughness [30] for applications. Ternary phase diagram shows that c-ZrO_2 + $RETaO_4$ two-phase field offers a possible pathway for enhancing toughness by the addition of a second phase. For $RE_{50}Ta_xZr_{50-x}$ systems, our experiments show that the microstructure of c-ZrO_2 + $RETaO_4$ can be obtained when x increases to 30 and 40. The measured penetration depths in Table 5 and the corrosion microstructures in Figs. 6(c)−9(c) and Figs. 6(d)−9(d) show that c-ZrO_2 + $RETaO_4$ two-phase fields in $RE_{50}Ta_{30}Zr_{20}$ (RE=Y, Dy, Gd) and $RE_{50}Ta_{20}Zr_{30}$ (RE=Dy, Gd) systems are effective to resist CMAS attack because their infiltration depths are narrow and the dense reaction layers can be generated. The dense reaction layer, which is formed by the mixture of apatite and pyrochlore phases, is very important to block further CMAS penetration. Because the formation abilities of apatite and pyrochlore phases are weak for Yb^{3+} and Y^{3+}, the dense reaction layers cannot be formed in $Yb_{50}Ta_{30}Zr_{20}$, $Yb_{50}Ta_{40}Zr_{10}$ and $Y_{50}Ta_{40}Zr_{10}$ systems. Therefore, our experimental results suggest that the Y, Dy and Gd dopants with larger ionic radiuses are applicable to obtaining an effective resistance to CMAS corrosion when their compositions are located in the two-phase region. On the contrary, $Yb_{50}Ta_xZr_{50-x}$ and $Y_{50}Ta_xZr_{50-x}$ with high $TaO_{2.5}$ contents are not suitable to resist CMAS corrosion.

4.3 Comparison of interaction experiments and CMAS penetration experiments

In the present work, interaction experiments and CMAS penetration experiments were both performed. Interaction experiments of phase equilibrium between CMAS and TBOs are effective to analyze chemical reactions and understand possible reaction products during CMAS penetration. In this work, the CMAS melt is sufficient and some residual glass phases are existent after interaction experiments. However, the amount of CMAS is not always sufficient during CMAS penetration. On the surface of TBO or TBC, the amount of CMAS is sufficient. As infiltration depth increases, the ratio of CMAS/TBO decreases. Therefore, at the interface between the corroded and uncorroded areas the chemical reaction products may be different in comparison with those on the surface. Some differences between interaction experiments and CMAS penetration experiments are significant and should be noted. Taking $Y_{50}Ta_{40}Zr_{10}$ as an example, interaction experiment in Fig. 3(d) shows that the reaction products are the pyrochlore phases, and some YT phases are residual. However, CMAS penetration experiment exhibits that three different reaction layers can be distinguished in Fig. 7(d). The single-pyrochlore phases are formed at the top of sub-layer, and the mixture of residual YT phases and pyrochlore phases can be observed in the middle sub-layer. The mixture of residual YT, pyrochlore and apatite phases can be found in the bottom sub-layer. Interaction experiments can only explain the observed penetration of the sub-layer in the middle area. Besides, the multi-layered penetration micro-structures can be also seen in Figs. 7(c), 8(c, d) and 9(c, d). In these pictures, the top layer contains pyrochlore phases and the layer near the reaction front contains the mixture of pyrochlore and apatite phases. The difference between interaction experiments and CMAS penetration experiments implies that comprehensive understanding of reaction products in the wide range of CMAS melts is essential to analyze the CMAS corrosion.

4.4 Resistance to CMAS corrosion in $RE_{50}Ta_xZr_{50-x}$ systems

According to our experimental data, the resistance characteristic to CMAS corrosion in $RE_{50}Ta_xZr_{50-x}$ systems can be classified into some categories. The difference is derived from the formation abilities of pyrochlore and apatite phases. For $Yb_{50}Ta_xZr_{50-x}$ systems, the resistance to CMAS corrosion is insufficient except for $Yb_{50}Ta_{10}Zr_{40}$ because no dense reaction layers can be formed after CMAS attack. For Yb-deficient systems with low $TaO_{2.5}$ content ($RE_{50}Ta_{10}Zr_{40}$), the dispersive fluorite and apatite phases can be produced due to the insufficient formation ability of pyrochlore phases. The dense reaction layers cannot be generated and the resistance to CMAS corrosion is weak. This is consistent with the reported results [17] that adding Ta^{5+} in $Y_4Zr_3O_{12}$ has detrimental effects on the CMAS mitigating ability. For $Y_{50}Ta_{40}Zr_{10}$, the residual $YTaO_4$ can hinder the formation of dense reaction layer and it is not resistant to CMAS penetration. For $Dy_{50}Ta_{20}Zr_{30}$, the chemical reaction after CMAS attack can take place along the grain boundary and it cannot prevent the CMAS infiltration. For other systems at higher content of $TaO_{2.5}$ than $RE_{50}Ta_{10}Zr_{40}$, CMAS penetration can result in the formation of the dense reaction layers, which contain pyrochlore and apatite phases. At the interface between the corroded and uncorroded areas, the pyrochlore and apatite phases are bound tightly together and can block further infiltration. In comparison with fluorite phases, the pyrochlore phases are easily combined with the apatite phases, which is attributed to that the morphology of pyrochlore phase is polygonal and angular. Accordingly, the formation ability of the dense reaction layer is decided not only by the amount of apatite phase, but also by the combined action of apatite and pyrochlore phases. This work suggests that the mixture of pyrochlore and apatite phases is a more effective approach to form the dense reaction layer, and exhibits the best resistance to CMAS corrosion.

5 Conclusions

(1) Higher $TaO_{2.5}$ contents in $RE_{50}Ta_xZr_{50-x}$ systems can suppress the nucleation of the apatite phase and increase the crystallization efficiency of the pyrochlore or fluorite phase. Formation abilities of apatite and pyrochlore phases are found to be proportional to the ionic radius of RE^{3+} (Gd^{3+}>Dy^{3+}>Y^{3+}>Yb^{3+}).

(2) The $c\text{-}ZrO_2 + RETaO_4$ two-phase field can be obtained when the content of $TaO_{2.5}$ in $RE_{50}Ta_xZr_{50-x}$ systems is more than 20 mol.%. The ability to mitigate CMAS corrosion was determined to be adequate for $c\text{-}ZrO_2$+$RETaO_4$ two-phase field. This is because the dense reaction layer can be

generated near the penetration front.

(3) The multi-layered microstructures can be observed in the CMAS penetration experiments. The difference of reaction products between interaction experiments and CMAS penetration experiments implies that the comprehensive understanding of reaction products in the wide range of CMAS melts is essential to evaluate the resistance characteristics to CMAS corrosion.

(4) The characteristics of the resistance to CMAS corrosion in $RE_{50}Ta_xZr_{50-x}$ systems are decided by the combined action of apatite and pyrochlore phases. The apatite phase is easier to combine with the angular pyrochlore phase than the spherical fluorite phase. The close-knit mixture of apatite and pyrochlore phases is more effective approach to form the dense reaction layer, and exhibits the best resistance to CMAS corrosion.

Acknowledgments

The work was supported by the National Natural Science Foundation of China (No. 51801170), the National Postdoctoral Program for Innovative Talents, China (No. BX20180265), the Natural Science Foundation of Hunan Province, China (No. 2019JJ50570), the China Postdoctoral Science Foundation (No. 2019M652786), and the Research Initiation Project of Xiangtan University, China (No. 18QDZ24).

References

[1] CLARKE D R, OECHSNER M, PADTURE N P. Thermal-barrier coatings for more efficient gas-turbine engines [J]. MRS Bulletin, 2012, 37: 891−898.

[2] PADTURE N P, GELL M, JORDAN E H. Thermal barrier coatings for gas-turbine engine applications [J]. Science, 2002, 296: 280−284.

[3] VOURDAS N, MARATHONITI E, PANDIS P K. Evaluation of $LaAlO_3$ as top coat material for thermal barrier coatings [J]. Transactions of Nonferrous Metals Society of China, 2018, 28: 1582−1592.

[4] HE M Y, HUTCHINSON J W, EVANS A G. Large deformation simulations of cyclic displacement instabilities in thermal barrier systems [J]. Acta Materialia, 2002, 50: 1063−1073.

[5] EVANS A G, CLARKE D R, LEVI C G. The influence of oxides on the performance of advanced gas turbines [J]. Journal of the European Ceramic Society, 2008, 28: 1405−1419.

[6] SONG Xue-Mei, ZHANG Ji-Mei, LIU Zi-Wei, JIANG Cai-Fen, LIN Chu-Cheng, ZENG Yi. Thermal shock resistance of YSZ, YSZ−Al_2O_3 and YSZ−Al_2O_3/YSZ coatings [J]. Vacuum, 2019, 162: 150−155.

[7] VASSEN R, CAO X Q, TIETZ F, BASU D, STÖVER D. Zirconates as new materials for thermal barrier coatings [J]. Journal of the American Ceramic Society, 2004, 83: 2023−2028.

[8] LEVI C G, HUTCHINSON J W, VIDAL-SETIF M H, JOHNSON C A. Environmental degradation of TBCs by molten deposits [J]. MRS Bulletin, 2012, 37: 932−941.

[9] ZHANG X F, NIU S P, DENG Z Q, LIU M, LI H, DENG C M, DENG C G, ZHOU K S. Preparation of Al_2O_3 nanowires on 7YSZ thermal barrier coatings against CMAS corrosion [J]. Transactions of Nonferrous Metals Society of China, 2019, 29: 2362−2370.

[10] KRÄMER S, FAULHABER S, CHAMBERS M, CLARKE D R, LEVI C G, HUTCHINSON J W, EVANS A G. Mechanisms of cracking and delamination within thermal barrier systems in aero-engines subject to calcium−magnesium−alumino−silicate (CMAS) penetration [J]. Materials Science and Engineering A, 2008, 490: 26−35.

[11] SONG W J, LAVALLÉE Y, HESS K U, KUEPPERS U, CIMARELLI C, DINGWELL D B. Volcanic ash melting under conditions relevant to ash turbine interactions [J]. Nature Communications, 2016, 7: 10795.

[12] PUJOL G, ANSART F, BONINO J, MALIÉ A, HAMADI S. Step-by-step investigation of degradation mechanisms induced by CMAS attack on YSZ materials for TBC applications [J]. Surface and Coatings Technology, 2013, 237: 71−78.

[13] GLEDHILL A D, REDDY K M, DREXLER J M, SHINODA K, SAMPATH S, PADTURE N P. Mitigation of damage from molten fly ash to air-plasma-sprayed thermal barrier coatings [J]. Materials Science and Engineering A, 2011, 528: 7214−7221.

[14] MECHNICH P, BRAUE W. Solid-state CMAS corrosion of an EB-PVD YSZ coated turbine blade: Zr^{4+} partitioning and phase evolution [J]. Journal of the American Ceramic Society, 2015, 98: 296−302.

[15] POERSCHKE D L, BARTH T L, LEVI C G. Equilibrium relationships between thermal barrier oxides and silicate melts [J]. Acta Materialia, 2016, 120: 302−314.

[16] POERSCHKE D L, JACKSON R W, LEVI C G. Silicate deposit degradation of engineered coatings in gas turbines: Progress toward models and materials solutions [J]. Annual Review of Materials Research, 2017, 47: 297−330.

[17] ABDUL-JABBAR N M, FERNANDEZ A N, JACKSON R W, DAESUNG D, SUMMERS W D, LEVI C G. Interactions between zirconia–yttria–tantala thermal barrier oxides and silicate melts [J]. Acta Materialia, 2020, 185: 171−180.

[18] JACKSON R W, ZALESKI E M, POERSCHKE D L, HAZEL B T, BEGLEY M R, LEVI C G. Interaction of molten silicates with thermal barrier coatings under temperature gradients [J]. Acta Materialia, 2015, 89: 396−407.

[19] ZALESKI E M, ENSSLEN C, LEVI C G. Melting and crystallization of silicate systems relevant to thermal barrier coating damage [J]. Journal of the American Ceramic Society, 2015, 98(5): 1−8.

[20] KRÄMER S, YANG J, LEVI C G, JOHNSON C A.

Thermochemical interaction of thermal barrier coatings with molten CaO−MgO−Al_2O_3−SiO_2 (CMAS) deposits [J]. Journal of the American Ceramic Society, 2006, 89(10): 3167−3175.

[21] KRÄMER S, YANG J, LEVI C G. Infiltration-inhibiting reaction of gadolinium zirconate thermal barrier coatings with CMAS melts [J]. Journal of the American Ceramic Society, 2008, 91(2): 576−583.

[22] AYGUN A, VASILIEV A L, PADTURE N P, MA X. Novel thermal barrier coatings that are resistant to high-temperature attack by glassy deposits [J]. Acta Materialia, 2007, 55: 6734−6745.

[23] DREXLER J M, ORTIZ A L, PADTURE N P. Composition effects of thermal barrier coating ceramics on their interaction with molten Ca−Mg−Al−silicate (CMAS) glass [J]. Acta Materialia, 2012, 60: 5437−5447.

[24] POERSCHKE D L, LEVI C G. Effects of cation substitution and temperature on the interaction between thermal barrier oxides and molten CMAS [J]. Journal of the European Ceramic Society, 2015, 35: 681−691.

[25] PITEK F M, LEVI C G. Opportunities for TBCs in the ZrO_2−$YO_{1.5}$−$TaO_{2.5}$ system [J]. Surface and Coatings Technology, 2007, 201: 6044−6050.

[26] MACAULEY C A, FERNANDEZ A N, LEVI C G. Phase equilibria in the ZrO_2−$YO_{1.5}$−$TaO_{2.5}$ system at 1500 °C [J]. Journal of the European Ceramic Society, 2017, 37: 4888−4901.

[27] SHIAN S, SARIN P, GURAK M, BARAM M, KRIVEN W M, CLARKE D R. The tetragonal−monoclinic, ferroelastic transformation in yttrium tantalate and effect of zirconia alloying [J]. Acta Materialia, 2014, 69: 196−202.

[28] SHEN Y, LECKIE R M, LEVI C G, CLARKE D R. Low thermal conductivity without oxygen vacancies in equimolar $YO_{1.5}$+$TaO_{2.5}$- and $YbO_{1.5}$+$TaO_{2.5}$-stabilized tetragonal zirconia ceramics [J]. Acta Materialia, 2010, 58: 4424−4431.

[29] MACAULEY C A, FERNANDEZ A N, van SLUYTMAN J S, LEVI C G. Phase equilibria in the ZrO_2−$YO_{1.5}$−$TaO_{2.5}$ system at 1250 °C [J]. Journal of the European Ceramic Society, 2018, 38: 4523−4532.

[30] LECKIE R M. Fundamental issues regarding the implementation of gadolinium zirconate in thermal barrier systems [D]. Barbara, Santa Barbara, CA: University of California Santa, 2006.

[31] ZHANG F, ZHANG G J, YANG L, ZHOU Y C, DU Y. Thermodynamic modeling of $YO_{1.5}$−$TaO_{2.5}$ system and the effects of elastic strain energy and diffusion on phase transformation of $YTaO_4$ [J]. Journal of the European Ceramic Society, 2019, 39: 5036−5047.

[32] ISTOMIN S Y, DYACHENKO O G, ANTIPOV E V. Synthesis and characterization of reduced niobates $CaLnNb_2O_7$, Ln=Y, Nd with a pyrochlore structure [J]. Materials Research Bulletin, 1997, 32: 421−430.

[33] POERSCHKE D L, SHAW J H, VERMA N, ZOK F W, LEVI C G. Interaction of yttrium disilicate environmental barrier coatings with calcium−magnesium−iron alumino−silicate melts [J]. Acta Materialia, 2018, 145: 451−461.

$RE_2Zr_2O_7$−$RETaO_4$体系中$RE_{50}Ta_xZr_{50-x}O_{175+0.5x}$热障涂层氧化物的抗 CMAS 腐蚀特征

龚闪闪，陈 明，黄勋鹏，张 帆

湘潭大学 材料科学与工程学院，湘潭 411105

摘　要：研究$RE_2Zr_2O_7$−$RETaO_4$体系中富稀土$RE_{50}Ta_xZr_{50-x}O_{175+0.5x}$氧化物在 1300 ℃下抗钙镁铝硅酸盐(CMAS)腐蚀特征，并讨论RE^{3+}和Ta^{5+}离子对 CMAS 熔体腐蚀化学反应和反应结晶的影响。结果表明，伴随着热化学反应，磷灰石、烧绿石、再沉淀的萤石和过剩的 Yb(Y)TaO_4相是主要的反应产物。磷灰石相和烧绿石相的形成能力与稀土离子半径成正比。Ta^{5+}含量的增加能减少形成磷灰石相的稀土原子的有效数目。此外，$RE_{50}Ta_xZr_{50-x}O_{175+0.5x}$热障涂层氧化物的抗 CMAS 腐蚀能力由磷灰石相和烧绿石相共同决定。紧密混合的磷灰石和烧绿石相在腐蚀反应的前端产生致密的反应层，该结构能够抑制 CMAS 的继续渗透。萤石和$RETaO_4$的两相组织能够有效地阻碍 CMAS 的腐蚀。

关键词：热障涂层；CMAS 腐蚀；热化学反应；磷灰石；烧绿石；渗透实验

(Edited by Wei-ping CHEN)